ASTFE
American Society
of Thermal and Fluids Engineers

5th-6th Thermal and Fluids Engineering Conference (TFEC)
May 26–28, 2021
Virtual Conference

TFEC-2020-36777

FULLY-COUPLED THERMAL-ELECTRIC-MECHANICAL MODELING OF THERMAL-ELECTRIC GENERATORS

Shane P. Riley,[1] Edward M. Ledesma,[1] Kevin Yu,[2] Fivos Drymiotis,[2] Matthew M. Barry[1,*]

[1]Department of Mechanical Engineering and Materials Science,
University of Pittsburgh, Pittsburgh, PA 15261, USA
[2]Jet Propulsion Laboratory, California Institute of Technology,
4800 Oak Grove Drive, Pasadena, CA 91109, USA

ABSTRACT

The development of improved power generation systems to support NASA's future deep-space exploration missions requires multi-faceted modeling to evaluate both the thermal-electric and thermal-mechanical performance of the thermal-electric generators (TEGs). To better determine generator characteristics that could meet mission needs, a fully-coupled thermal-electric-mechanical numerical model was developed in ANSYS Mechanical and ANSYS CFX via user-defined subroutines. All pertinent thermal-electric phenomena, namely the Joule, Peltier, Thomson and Bridgman heats, were coupled to the general heat transport equation via volumetric and surface source terms. The electric potential and current density were simultaneously solved for using the Electromagnetics Model within ANSYS CFX, and said quantities evolved implicitly with the solution, as to provide the necessary boundary conditions for Maxwell's equations. Thermal expansion was modeled using a Boussinesq approximation and was coupled to the heat and thermal-electric equations via the inherent geometric dependence of thermal-electric phenomena. Deformation based on thermal expansion was handled through an iterative re-meshing routine, and was investigated under free-floating, spring-loaded, and constrained system configurations. Said deformation was used to determine stresses generated within each component of the TEG via ANSYS Mechanical. All thermo-physical materials were treated as temperature-dependent. Insight into the thermal-electric and thermal-mechanical performance of a unicouple, with and without interfacial compliance materials, under the influence of thermal loading was gained.

KEY WORDS: finite volume, fully-coupled, thermal-electric-mechanical, thermal deformation

INTRODUCTION

Thermal-electric devices (TEDs) utilize a temperature difference across semiconducting materials to create electrical power [1]. When used to generate power using the Seebeck effect, these devices are also referred to as thermal-electric generators (TEGs). The thermal conversion efficiency of such devices is too low for them to be competitive in large-scale power generation, typically ranging between 4-8% [2]. While this is the case, TEGs have several design advantages over other power generation methods – small size, solid-state operation, and long operational lifetimes – that make them useful in certain applications. Two of these applications are terrestrial waste heat recovery and extra-terrestrial power generation. For deep-space power generation applications, TEGs provide power where solar power is impractical or infeasible. In deep-space power generation applications, it is necessary for TEGs to be able to withstand thermal stresses from the heat source and remain functional in a thermally-deformed state.

*Corresponding Matthew M. Barry: matthew.michael.barry@pitt.edu

TEG performance is dependent on the consistency of the input heat flux and subsequent temperature gradient imparted across the device, the thermal-electric (TE) materials comprising the generator, and the geometric design of the TEG itself. In space power generation, the input heat flux tends to be pseudo steady-state and well-defined, considering a radioisotope thermal-electric generator in its long-term operational environment [3]. The selection of semiconducting materials for power generation is a major factor in TEG design. Materials with a high Seebeck coefficient, α_S, low electrical resistivity, ρ, and low thermal conductivity, λ, are favorable because they produce more power for a given heat flux and tend to reach greater power densities and conversion efficiencies [4, 5]. To capture the effects of all three properties together on a material's performance, a dimensionless figure of merit, $Z\overline{T}$ is expressed in terms of the Seebeck coefficient of the n- and p-type materials, and their respective electrical resistance and thermal conductance [6], such that

$$Z\overline{T} = \frac{\alpha_S^2 \overline{T}}{R_{el} K} \tag{1}$$

It is noted that in the expression for the figure of merit, the variables within the denominator, electrical resistance, R_{el} and thermal conductance, K, take into account geometric parameters of the thermal-electric element legs [7]. Materials with a higher $Z\overline{T}$ are more capable of producing power for a given heat flux. All material properties are dependent on temperature difference across the junctions, leading to various device designs for optimization. This includes segmented-TEGs [8–10] and multi-stage TEGs [11, 12]. The present work uses publicly-sourced temperature dependent material properties for the n- and p-type semiconductors. However, the proposed model herein is applicable to all TE materials because its primary focus is on capturing thermal-electric/thermo-mechanical performance for a range of geometries and materials.

While the figure of merit is vital in understanding the thermal-electric performance of TEGs, additional material properties and device design factors must be taken into account when considering the durability of such devices. TEGs used in space power generation experience a wide range of temperature differences, sometimes in excess of 500 K [3]. Such extreme conditions can bring into question the durability of these devices, necessitating further testing and modelling of these thermo-mechanical effects. For example, Ziolkowski et al. created numerical models of TEGs using the ANSYS Parametric Design Language (APDL) [13]. Karri et al. used similar techniques to capture the effects of different constraints and leg shapes on the structural performance of TEGs [14]. Additionally, Ziabari et al. examined the effects of different design choices on the shear stresses experiences at the interfaces in TEG components [15].

To build upon prior works, an alternative coupled-model method is presented, which uses ANSYS Workbench, as well as ANSYS CFX, in which thermal-electric performance characteristics are quantified. The use of ANSYS CFX allows for the inclusion of all thermal-electric phenomena (including Bridgman heating) via a fully-implicit multi-physics solution algorithm and CEL expressions. The thermal-electric model implemented in ANSYS CFX provides temperature distributions within the TEG that are then used in ANSYS Mechanical to determine the resulting thermal deformation of the TEG. Upon deformation, a new mesh is created, and the ANSYS CFX model is re-solved, such that the effects of deformation on thermal-electric performance can be determined. The proposed method is implemented using temperature-dependent thermal-electric and thermo-mechanical properties. To demonstrate said method, an unsegmented single couple geometry is modelled under free, fixed, and variable elastic constraints. A contact compliance material (CCM) is then added in an attempt to decrease the maximum stresses experienced by the TE couple under thermal load. The following models are constructed using ANSYS 17.2.

METHODOLOGY

A schematic of the solution methodology is presented in Fig. 1 a), and will be elaborated upon in the following. To create deformed geometries for thermal-electric modelling in the thermo-mechanical coupled model, it is necessary to use a geometry generation scheme that allows for the TEG dimensions to be adjusted in

scripting. ANSYS ICEM CFD was chosen for this purpose because it makes use of replay files to reconstruct geometries and meshes. By starting with a generalized template file for a geometry and mapping mid-solve point deformations to it, it is possible to generate geometries that account for the thermal deformation of the couple. To create the template model, a network of capture points is used to build the geometry within ICEM CFD. These capture points are shown as the black dots in Fig. 1 b). The movement of these points will be captured by the mechanical post-processor and passed back into the tool to generate a new geometry for thermal-electric modelling. The number of vertices in the model is the minimum number of capture points necessary to create a fully regenerative model, but additional points can be used along edges to capture curvature.

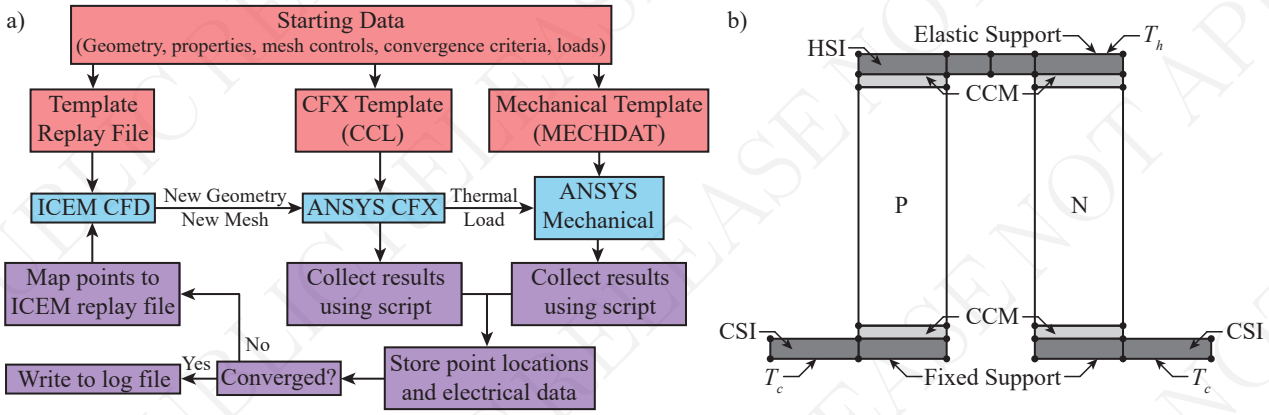

Fig. 1 Representation of a) a programmatic flow chart, and b) a TEG geometry with CCM and capture points.

The thermal-electric performance of the TE single-couple is captured using ANSYS CFX. The solver makes use of CEL-expressions within CFX to evaluate temperature-dependent material properties, induced thermal-electric voltage, and heats from the Peltier, Thomson, and Bridgmann effects (Joule heating is handled by CFX internally). These expressions are linked to the leg domains as volumetric/interfacial sources for evaluation throughout. Further explanation of the calculation of heats and the CFX model is provided by Ledesma et al. on executing performance modelling within the fluids solver [16]. The same methodology for the performance modelling portion is used here.

Using a template file and the generated mesh for a given cycle, the thermal-electric performance modelling takes place within ANSYS CFX. Once the thermal-electric performance solution is completed, the body-temperature map from the CFX result is passed into ANSYS Mechanical using the one-way mapping utility provided by ANSYS Workbench. In subsequent cycles of the model, as additional thermal profiles accumulate, all are applied in a load-stepping fashion to the structural model, which always starts with the undeformed TE couple geometry. Additional constraints are then applied to the structural model, namely a fixed constraint on the cold side interconnectors (CSI) and an elastic constraint on the hot side interconnector (HSI), the stiffness of which can be adjusted. The effect of this stiffness on the resulting stresses in the TE couple will be observed using the coupled modelling technique described.

To prepare the model for simulation in the prepared framework, material properties, loads, and post-processor controls are put into ANSYS ICEM, CFX, and Mechanical template files for import into Workbench. These templates are referred to by the main macro, which is a Workbench journal executed using a run flag on startup of Workbench. The geometry prepared is a generic TE single couple, with two 10.00 mm long by 1.00 mm thick by 5.00 mm wide CSIs, one 15.00 mm long by 1.00 mm thick by 5.00 mm wide HSI, and two legs with cross sections of 5.00 mm by 5.00 mm and heights of 10.00 mm. When the CCM layer is applied between the HSI and the TE legs, it is of thickness 0.25 mm. A load resistance of 20.0 μΩ is applied, and a temperature difference of 300 K is placed across the TE couple, with the cold side set to 304 K. As per previous grid independence studies on the given geometry, a mesh size of 50 μm is appropriate for the thermal-electric performance model. A mesh size of 250 μm is applied to the Mechanical model, since the captured mechanical

deformation precision is limited by the number of capture points generating the geometry. Additionally, the structural mesh with the CCM layer will use a smaller sizing on the nickel material (five elements across the interface). This will allow for a more accurate examination of the layers' effect on leg stress. Finally, a convergence criterion is applied to the model: if no capture points move more than 10 μm from iteration to iteration, the model is considered converged. This convergence criterion is applied in the Workbench journaling script. A mapping of the thermal load is shown in Figure 2.

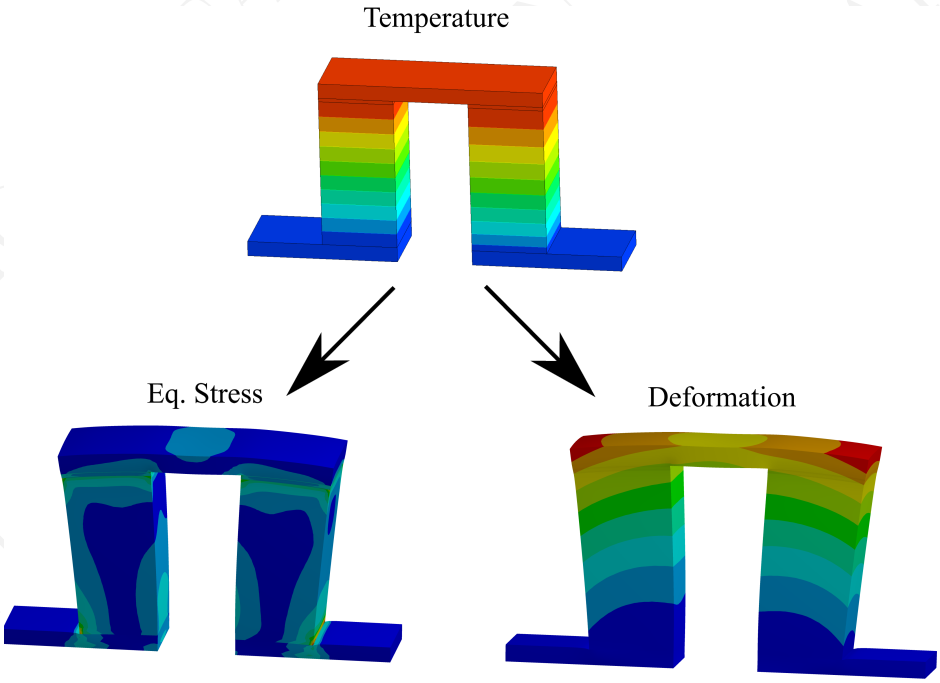

Fig. 2 Mapping temperature to obtain thermal deformation and equivalent stress.

Material properties for the metal interconnectors, CCM layer, and n- and p-type legs are established as temperature dependent. The data is presented in Tabs. 1 and 2. Since the thermal-electric properties are input as a function of temperature into ANSYS CFX, an eighth-order polynomial fit is constructed to effectively capture the behavior of the properties in the range of 300 to 650 K. The thermo-mechanical properties are added to the structural model using Workbench Engineering Data, which handles linear interpolation internally [17–19]. Some values for elastic modulus and Poisson's ratio are taken as temperature-independent in the analysis due to lack of available properties. The model is capable of using temperature-dependent values for these properties given their availability.

Table 1 Temperature-dependent n- and p-type thermal-electric material properties.

Coefficient T^x	$\alpha_{S,p}$ (V K^{-1})	ρ_p (Ω m)	λ_p (W m^{-1} K^{-1})	$\alpha_{S,n}$ (V K^{-1})	ρ_n (Ω m)	λ_n (W m^{-1} K^{-1})
0	7.6254e-05	3.5455e-04	2.1727	-3.8424e-05	8.8341e02	-7.2225
1	8.2209e-08	3.8346e-07	1.0262e-03	-9.5087e-08	6.3860e-01	6.6457e-01
2	-1.1601e-08	-2.9537e-08	-2.6517e-31	1.6046e-09	4.4790e-02	-2.3617e-03
3	1.1882e-10	3.3221e-10	-8.3596e-08	2.9312e-11	-5.1559e-04	4.1317e-06
4	-4.9366e-13	-1.5189e-12	7.4551e-10	-1.7651e-13	2.2826e-06	-3.5455e-09
5	1.0788e-15	3.6269e-15	-2.5747e-12	4.9602e-16	-5.3707e-09	1.1952e-12
6	-1.3108e-18	-4.7728e-18	4.3139e-15	-7.2655e-19	7.0825e-12	0
7	8.3947e-22	3.2849e-21	-3.5249e-18	5.4159e-22	-4.9481e-15	0
8	-2.2126e-25	-9.2555e-25	1.1295e-21	-1.6294e-25	1.4264e-18	0

Structural measurements for the TE couples consist of maximum principal stress measurements taken 50 μm

Table 2 Temperature-dependent CCM layer, interconnector, n- and p-type thermo-mechanical properties.

	Interconnector			CCM Layer		
Temperature (K)	E_{int} (GPa)	ν_{int} (-)	$\alpha_{T,int}$ 10^{-6} (-)	E_{ccm} (GPa)	ν_{ccm} (-)	$\alpha_{T,ccm}$ 10^{-6} (-)
200	133	0.341	15.0	-	-	11.0
250	-	-	16.0	-	-	12.6
300	-	-	16.6	-	-	12.6
350	-	-	17.0	-	-	13.0
400	120	0.346	17.5	-	-	13.4
450	-	-	17.7	-	-	13.9
500	-	-	18.0	-	-	14.3
550	-	-	18.4	-	-	14.5
600	109	0.352	18.7	180	0.34	14.8
	p-type			n-type		
Temperature (K)	E_p (GPa)	ν_p (-)	$\alpha_{T,p}$ 10^{-6} (-)	E_n (GPa)	ν_n (-)	$\alpha_{T,n}$ 10^{-6} (-)
341	436	0.29	11.3	436	0.29	11.2
391	-	-	11.5	-	-	11.4
441	-	-	11.7	-	-	11.8
492	-	-	11.9	-	-	12.0
542	-	-	12.1	-	-	12.2
593	-	-	12.4	-	-	12.3
634	-	-	12.6	-	-	12.5

from the top of the n and n-type legs. The samples taken along the path are then averaged. The maximum arch deformation is measured using a directional deformation path along the top surface of the HSI. Finally, the movement of each point is captured using three user-defined results in ANSYS Mechanical − one for each axis − and the data is sent to Workbench using Design Point parameters for easy retrieval by the journal script. Measurements of thermal-electric performance are taken using ANSYS CFD-Post on the last cycle of the model.

RESULTS AND DISCUSSION

The proposed model was implemented to determine the effect of the elastic support stiffness and the inclusion of a CCM layer on the maximum principal stresses generated within the TE legs, the magnitude of the HSI deflection, and the subsequent thermal-electric performance of a single couple. To begin, the elastic support stiffness was varied between 0 (free) and 5,000 N/mm^3, and the maximum principal stress in the n and p-type legs was measured, as shown in Fig. 2 a) and b), respectively. For reference, the zero-strain temperature of the TE leg is 22 degrees C. It is immediately evident that increasing the stiffness of the elastic support near-linearly increases the maximum principal stresses in both the n and p-type legs. Furthermore, the inclusion of the CCM layer near-constantly decreases the maximum principal stresses by 11% in the n-type leg and 12% in the p-type leg.

Next, the deflection of the HSI as a function of the elastic support loading could be examined, with results shown in Fig. 3 a). In the unconstrained case, deflection of the HSI is at a maximum, and the maximum arch deformation occurs at the middle of the HSI as it deflects upward, as shown in Fig. 3 b). When the elastic constraint's stiffness is increased, however, the middle of the interconnector undergoes deflection in the opposite direction, as evidenced in Fig. 3 b), which will result in a substantial stress in the region of high deformation gradients. There is a clear relation between HSI deformation as shown in Fig. 3 b) and maximum principal stresses within the TE legs as shown in Fig. 3 a). As the HSI is unable to deform upwards, i.e. there is an increase in the elastic support stiffness, the principal stresses within the TE legs increase. Furthermore,

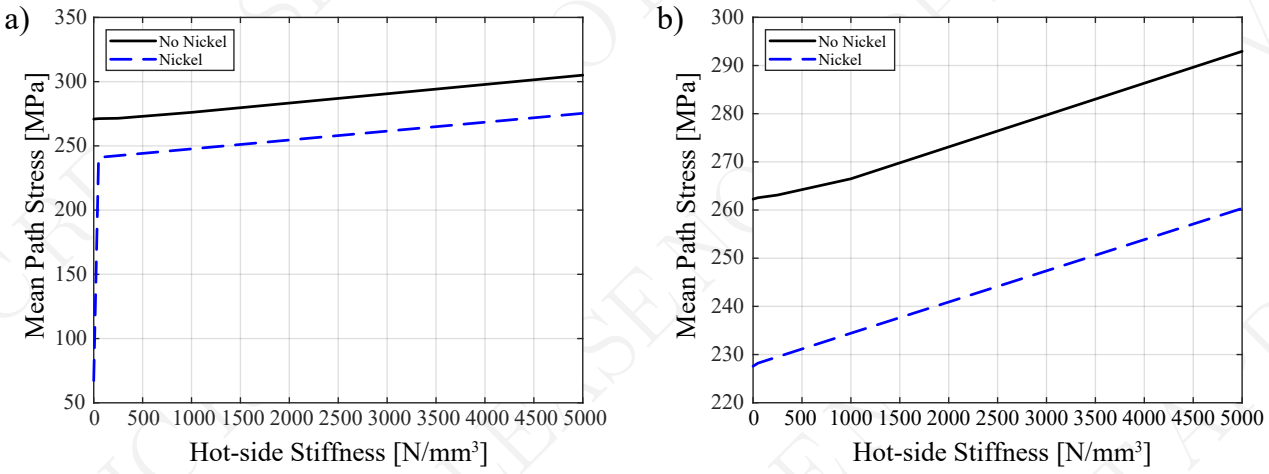

Fig. 3 Maximum principal stress in the a) n-type leg and b) p-type leg, with and without nickel CCM layer.

with a greater temperature difference imposed across the generator, the deformation of the HSI and subsequent imparted stresses within the TEG will increase. Thus, it is imperative to incorporate compliance into the HSI, especially at higher-temperature scenarios.

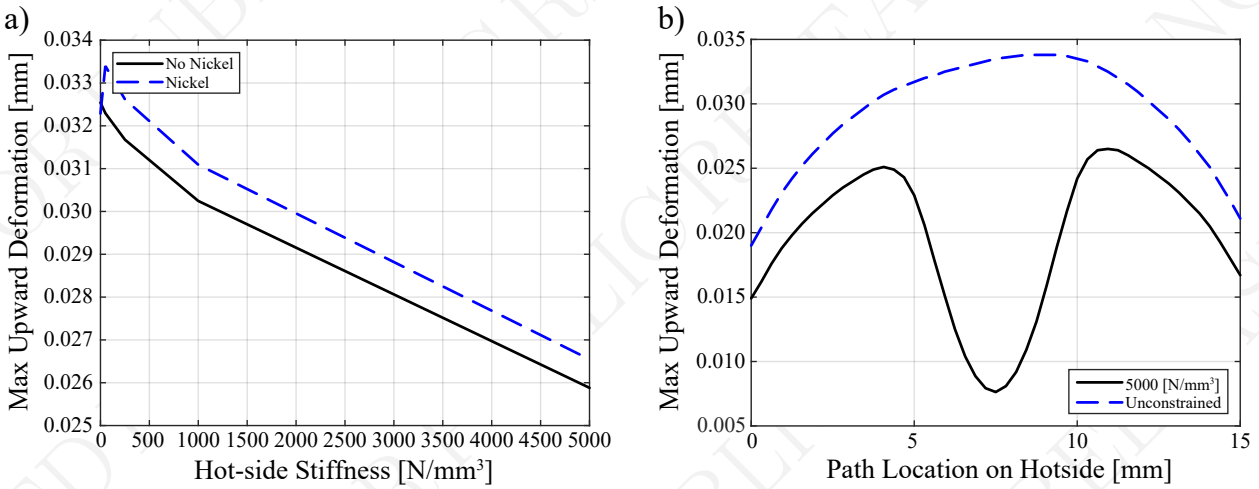

Fig. 4 Maximum a) upward deflection of the HSI with and without a CCM layer and b) path deflection of the HSI on the no-CCM model, with and without a stiff elastic constraint.

Additionally, the effect of mechanical deformation on thermal-electric performance was able to be determined. For a TED allowed to freely expand on the hot side interconnector, the TE leg lengths increase by only 0.2% for a thermal load of 300 K, and the generated electric current decreases by about 1%. This is due to the increase of electrical resistance of the TE legs due to the slight increase in length. With an elastic constraint of 5,000 N/mm^3, however, the generated current decreases by less than a tenth of a percent. It is expected that applying a larger thermal load on the legs (500 K or more) will cause a greater change in this value for current.

Considering all scenarios under which the proposed model was tested, said model converged in two cycles given the specified convergence criteria. This rapid convergence is attributable to fact that the thermal characteristics of the TEG change minimally after the first cycle of the model. That is to say, without significant deformation, there will be insignificant changes to the thermal-electric material properties, namely electrical resistance and thermal conductance of the legs, due to the treatment of the electrical resistivity and thermal conductivity via a Boussinesq approximation. Additionally, the imparted temperature difference of 300 K is

relatively small in terms of eliciting thermal deformation. It is expected that using a higher temperature difference (500 to 1,000 K) will require more cycles to reach the specified convergence criteria. With that being said, the proposed model allows for the rapid thermal-electric-mechanical coupled modeling of TEGs, such that the effects of thermal deformation on thermal-electric performance can be evaluated.

CONCLUSIONS

The proposed fully-coupled thermal-electric-mechanical model of TE couples, although more computationally expensive than segregated thermal-electric and thermal-mechanical models due to the iterative re-meshing scheme, has the ability to simultaneously quantify the effects of thermal-induced deformations on the mechanical behavior and thermal-electric performance on device performance. Specifically, a TE couple with a free-floating HSI experiences the least amount of principal stresses generated within the TE materials, sees the greatest deflection of the HSI, as well as experiences the greatest change of thermal-electric performance. As the stiffness of the elastic support increases, the principal stresses with the TE materials increase, the deformation of the HSI decreases, and the thermal-electric performance changes substantially decrease. It is also found that the inclusion of a CCM layer substantially decreases the maximum principal stresses within the TE couple as well as the deformation of the HSI. The proposed model can rapidly evaluate the suitability of various TE and CCM materials, as well as TEG designs, for a diverse set of TEG applications.

ACKNOWLEDGMENTS

The authors would like to thank Solomon Fenton of the University of Pittsburgh for his assistance in procuring material properties. Computational resources and support were provided by the Center for Research Computing (CRC) at the University of Pittsburgh.

NOMENCLATURE

Variables

E	Elastic modulus	(GPa)	R_{el}	Electrical resistance	(Ω)
K	Thermal conductance	(WK^{-1})	T	Temperature	(K)
n	n-type		ZT	Dimensionless figure of merit	(-)
p	p-type				

Subscripts and Superscripts

c	Cold side	ccm	CCM Layer
int	Interconnector	p	p-type
h	Hot side	x	Order of coefficient
n	n-type		

Greek Letters

α_S	Seebeck coefficient	(VK^{-1})	ν	Poisson's Ratio	(-)
α_T	Coefficient of thermal expansion	(-)	ρ	Electrical resistivity	(Ωm)
λ	Thermal conductivity	($\mathrm{Wm}^{-1}\mathrm{K}^{-1}$)			

Acronyms

CCM	Contact compliance material	TE	thermal-electric
CSI	Cold side interconnector	TED	thermal-electric device
HSI	Hot side interconnector	TEG	thermal-electric generator

REFERENCES

[1] T. J. Seebeck, "Ueber die magnetische polarisation der metalle und erze durch temperaturdifferenz," *Annalen der Physik*, vol. 82, no. 3, pp. 253–286, 1826.

[2] Y. Wu, J. Yang, S. Chen, and L. Zuo, "Thermo-element geometry optimization for high thermoelectric efficiency," *Energy*, vol. 147, pp. 672–680, 2018.

[3] G. Bennett, J. Lombardo, R. Hemler, G. Silverman, C. Whitmore, W. Amos, E. Johnson, A. Schock, R. Zocher, T. Keenan, *et al.*, "Mission of daring: the general-purpose heat source radioisotope thermoelectric generator," in *4th International Energy Conversion Engineering Conference and Exhibit (IECEC)*, p. 4096, 2006.

[4] E. Altenkirch, "Über den nutzeffekt der thermosäule," *Physikalische Zeitschrift*, vol. 10, pp. 560–580, 1909.

[5] E. Altenkirch, "Elektrothermische kälteerzeugung und reversible elektrische heizung," *Physikalische Zeitschrift*, vol. 12, pp. 920–924, 1911.

[6] A. F. Ioffe, *Semiconductor thermoelements and thermoelectric cooling*. Infosearch London, 1957.

[7] S. W. Angrist, *Direct Energy Conversion*. Allyn and Bacon Inc. (Boston), 4 ed., 1982.

[8] H. Tian, X. Sun, Q. Jia, X. Liang, G. Shu, and X. Wang, "Comparison and parameter optimization of a segmented thermoelectric generator by using the high temperature exhaust of a diesel engine," *Energy*, vol. 84, pp. 121–130, 2015.

[9] H. Ali and B. S. Yilbas, "Configuration of segmented leg for the enhanced performance of segmented thermoelectric generator," *International Journal of Energy Research*, vol. 41, no. 2, pp. 274–288, 2017.

[10] M. Zare, H. Ramin, S. Naemi, and R. Hosseini, "Exact optimum design of segmented thermoelectric generators," *International Journal of Chemical Engineering*, vol. 2016, 2016.

[11] R. Arora and R. Arora, "Multicriteria optimization based comprehensive comparative analyses of single-and two-stage (series/parallel) thermoelectric generators including the influence of thomson effect," *Journal of Renewable and Sustainable Energy*, vol. 10, no. 4, p. 044701, 2018.

[12] M. Zhou, Y. He, and Y. Chen, "Three-dimensional numerical modeling and characterization of two-stage and multilayer thermoelectric couples," *International Journal of Green Energy*, vol. 13, no. 7, pp. 736–746, 2016.

[13] P. Ziolkowski, P. Poinas, J. Leszczynski, G. Karpinski, and E. Müller, "Estimation of thermoelectric generator performance by finite element modeling," *Journal of electronic materials*, vol. 39, no. 9, pp. 1934–1943, 2010.

[14] N. K. Karri and C. Mo, "Structural reliability evaluation of thermoelectric generator modules: influence of end conditions, leg geometry, metallization, and processing temperatures," *Journal of Electronic Materials*, vol. 47, no. 10, pp. 6101–6120, 2018.

[15] A. Ziabari, E. Suhir, and A. Shakouri, "Minimizing thermally induced interfacial shearing stress in a thermoelectric module with low fractional area coverage," *Microelectronics Journal*, vol. 45, no. 5, pp. 547–553, 2014.

[16] E. M. Ledesma, S. Sammak, and M. M. Barry, "Modeling bridgman heating in thermoelectric generators," in *ASTFE Digital Library*, Begel House Inc., 2021.

[17] H. Ledbetter and E. Naimon, "Elastic properties of metals and alloys. ii. copper," *Journal of physical and chemical reference data*, vol. 3, no. 4, pp. 897–935, 1974.

[18] H. M. Ledbetter and R. P. Reed, "Elastic properties of metals and alloys, i. iron, nickel, and iron-nickel alloys," *Journal of Physical and Chemical Reference Data*, vol. 2, no. 3, pp. 531–618, 1973.

[19] F. Nix and D. MacNair, "The thermal expansion of pure metals: copper, gold, aluminum, nickel, and iron," *Physical Review*, vol. 60, no. 8, p. 597, 1941.